

Integrating multiple models into computational fluid dynamics for fine three-dimensional simulation of urban waterfront wind environments: A case study in Hangzhou, China

Weiwu Wang ^{a,*}, Huan Chen ^a, Lizhong Wang ^a, Shan Wang ^b

^a College of Civil Engineering and Architecture, Zhejiang University, Hangzhou 310058, China

^b Center for Balance Architecture, Zhejiang University, Hangzhou 310058, China



ARTICLE INFO

Keywords:

Fine three-dimensional (3D) simulation of ventilation
Urban waterfront area (UWA)
Porous media (PM)
Water-air interface exchange (WAIE)
Ventilation adaptive planning and design

ABSTRACT

A comfortable wind environment in urban waterfront area (UWA) is critical to improving the quality of life of surrounding residents and environment sustainability. In this study, the porous media model was combined with the water-air interface exchange model to conduct high-precision three-dimensional (3D) simulation of the ventilation environment at an urban waterfront. The results of this study indicate that the accuracy of the proposed model is as high as 95%. This model can be used to efficiently simulate urban ventilation and pedestrian wind environment comfort at different heights (1.5, 10, and 30 m) in a certain high-density 3D UWA. The order of ventilation potential of different types of urban areas is road space, green space, and river space. In summer, the pedestrian wind environment around the Gongshu section of the Beijing-Hangzhou Grand Canal was discovered to have low comfort at a height of 1.5 m. In winter, the wind comfort of the UWA on both sides of the canal is greatly affected by the direction of incoming wind, showing satisfactory ventilation performance when reaching heights of 10 and 30m. Accurate and efficient 3D simulation of urban ventilation is very helpful for adaptive planning and design of urban wind environment.

1. Introduction

Under the influence of environmental comfort awareness, the urban single-factor economic development cycle has gradually transformed into a "nature-society" dual-ecological social development cycle (Reyers & Selig, 2020; Liu et al., 2021). Therefore, emphasizing ecosystem factors (wind, water, green plants, etc.) as the driving mechanism for improving environmental quality has become an important proposition for the sustainable development of urban society (Andersen et al., 2021; Meng et al., 2016; Sebastian & Ellen, 2022). Urban water bodies are a crucial source of cooling in cities and weaken the urban heat island effect by cooling and humidifying the atmosphere (Syafii et al., 2016; Lin et al., 2020; Sun et al., 2020), bringing huge health benefits to city dwellers and becoming a space that city dwellers are willing to get close to. Therefore, urban planners are increasingly focusing on using urban water bodies to alleviate the increasingly severe wind- and heat-related problems in urban environments. In cities, dynamic and thermal effects are caused by changes in the underlying surface roughness, which has a complex composition (Wang, 1992). Because of the considerable

differences in the physical properties of water bodies and natural surfaces, such as those in woodlands and grasslands, versus artificial surfaces, such as those made of asphalt and masonry, land and water surfaces generate different atmospheric disturbances. Therefore, accurately analyzing the wind environment of complex urban three-dimensional (3D) spaces by using a single model is difficult. The wind environment of a waterfront is affected by meteorological conditions, such as temperature, humidity, wind speed, wind direction, and solar radiation. Moreover, the wind environment of rivers varies considerably across the different seasons. Therefore, research on the wind environment of urban waterfront area (UWA) should involve in-depth analysis of various dimensions.

The wind environment research conducted at the University of Western Australia is mainly focused on analyzing the effect of the layout patterns of buildings and blocks in a waterfront space on the water body's wind permeability (Meng & Li, 2015) and the effect of small water bodies on the wind environment of medium-sized residential areas from a two-dimensional perspective (Jin et al., 2017). Large amounts of data and numerous computations are required when using

* Corresponding author.

E-mail address: weiwuwang@zju.edu.cn (W. Wang).

computational fluid dynamics (CFD) technology to simulate the wind and heat environment of a UWA, and the 3D simulation of medium-scale wind and heat is relatively complex. Existing 3D simulation software for wind and heat environments cannot efficiently analyze 3D geographic information (Hang & Li, 2012). Studies have indicated that the use of a porous media (PM) model can effectively reduce the number of CFD calculations required for the aforementioned simulation (Zhang et al., 2016b). Therefore, a simplified PM model can result in high efficiency of CFD for simulating urban wind environments in UWA.

Based on the above background, this study proposed a new method of integrating a simplified PM model and a water-air interface exchange (WAIE) model into a CFD software program to achieve fine 3D wind field simulation in urban waterfront areas for the first time. The current study contributes to the literature on several points. First, this is the first study integrating a simplified PM model and a water-air interface exchange (WAIE) model into a CFD software, field data were collected for verifying the accuracy of the proposed integrated model. Second, the integrated model was used to analyze the measured data to obtain parameters related to the water-air interface, and then used to achieve a refined CFD simulation of the wind environment in Gongshu UWA, Hangzhou, China. Simulation results demonstrate that our proposed method doubles the time efficiency of the simulation compared to CFD simulations of real buildings with similar simulation accuracy. To provide a guideline for the achievement of adaptive design goals for urban waterfronts, this research is critical in providing wind-sensitive design to achieve sustainable development goals for wind comfort in urban communities. Third, this study is unique in the multi-model integration methods that produce more realistic and 3D reliable simulations, and some targeted strategies were developed for enhancing wind comfort in the UWA.

The following parts of this study are organized as is that literature review in Section 2, integration of the PM and WAIE models in Section 3, methodology and results of applying the developed integrated model to the case in Section 4, discussion in Section 5 and finally conclusion in Section 6.

2. Literature review

2.1. Effect of water bodies on an urban environment

Many studies have confirmed that the effect of a water body's temperature on the surrounding environment is influenced by the water body's type, surface area, depth, and other characteristics. According to Syafii et al. (2016), water bodies can weaken the heat island effect through evaporation and water vapor heat transfer. Xue et al. (2019) estimated the land surface temperatures of areas displayed in Landsat 8 thermal infrared images by using the segmented window algorithm and found that the cooling effect of rivers is considerably stronger than those of other wetland types and green spaces. By using an outdoor-scale model, Syafii et al. (2017) discovered that water bodies with larger surface area have stronger cooling effects. In addition, ambient air temperature, solar radiation, water temperature, urban form, and other factors all affect water bodies' cooling and humidification benefits. Hathway and Sharpies (2012) determined that the cooling effect of a water body is positively correlated with the ambient air temperature, season, river water temperature, incident solar radiation, wind speed, and relative humidity. Song, Liu, & Zhao (2017) found that the geometry and area of ventilation corridors in residential areas and land use can influence the cooling effect of water bodies. After using detailed field measurements to calculate the cooling intensity of the Cheonggye River in Seoul, South Korea, Park et al. (2017) found that the cooling effect of the river is stronger when the streets are narrower and the buildings around it are shorter. However, the results of many studies have indicated that the cooling effect of water bodies is limited to a certain distance. Cai et al. (2018) found that the cooling effect of a water body in Chongqing, Yuzhong District, China, can extend over a distance

of 1 km from the water body. On the basis of analysis of Landsat 5 Thematic Mapper images, Li et al. (2008a) concluded that the effective cooling range of rivers in an urban environment is approximately 200 m. According to Li et al. (2008b), the cooling effect of urban water bodies on the environment extends to less than 2 km upwind and less than 9 km downwind and is strongest within 2.5 km. Moreover, urban water bodies can increase the air humidity and wind speed in the surrounding environment. Jauregui (1990) discovered that newly constructed lakes and ponds increase the horizontal advection of moist air downwind, which increases the incidence of near-surface fog. Szucs (2013) used ENVI-met to simulate the microclimate of the Grand Canal Square within Dublin Docklands and found a 20% faster wind along the waterfront than elsewhere.

2.2. PM and WAIE models

PM are solid materials with tiny voids and have widespread applications in Earth science, mechanics, material science, construction engineering, and other fields (Prévost, 1980). In the PM model, the flow resistance in a porous medium (determined using an empirical formula) is used to reflect the turbulent flow resistance in a region (Madsen, 1974). Studies have indicated that the introduction of PM model can effectively reduce the amount of simulation calculation. Hang et al. (2012) considered an urban canopy with buildings and street networks to comprise PM and used a porous turbulence model to macroscopically examine the airflow in this canopy and thus predict the macroscopic average airflow through porous building arrays by performing relatively few computations. PM models, such as building tree parameter models, mainly focus on the microscopic level in their determinations of the diffusion of road pollutants. Salim, Heinke Schlünzen, & Grawe (2015) found that using the PM approach to include trees in numerical simulations of urban wind flow can significantly improve the simulation. Jeanjean et al. (2015) treated trees as PM and examined the effectiveness of trees in dispersing road traffic emissions within an urban area. They found that trees reduce road traffic emissions by an average of 7%. By using trees as PM, Zhang et al. (2016a) revealed that community greening can result in the effective adsorption and blockage of particulate matter.

Quantitative research on the microclimatic effects of waterfronts has mainly focused on material exchange between the water body and the atmosphere. Dalton's law, the energy balance method, and Penman's model are three classical tools for calculating the exchange of matter and energy at a water-air interface. In 1802 Dalton proposed that the extent of evaporation is proportional to the water vapor pressure difference. This statement is called Dalton's law, which is the basis of modern evaporation theory. The principle of energy balance was proposed by Schmidt in 1915 and has high applicability for small water bodies; however, obtaining the net radiation and sensible heat flux by using this principle is difficult. Bowen employed the ratio of sensible heat flux to latent heat flux to obtain the sensible heat flux in Nie & Qu (2017). Penman (1948) and Pu, P.M. (1994) developed a comprehensive model by combining the energy balance and mass transport methods. In this model, water surface evaporation is as defined as the weighted sum of the rates of evaporation caused by net radiation and turbulent transport. The coefficients of Penman's model were optimized by Priestley and Taylor (1972) and De Bruin & Keijman, 1979. Researchers have optimized Penman's model. Tanny et al. (2008) also optimized Penman's model and reported that the volume transfer coefficient at an air-water interface is strongly dependent on the wind speed.

Researchers have determined model coefficients. By using Dalton's formula, Pu (1994) determined the factors affecting water surface evaporation and their nonlinear interactions. Moreover, Peimin introduced new dimensionless parameters and formulas. By using the experimental data of 19 evaporation stations across China and the Bayangore evaporation station, Li (2000) determined, with high accuracy, the parameters of a model for water surface evaporation. Min

(2005) proposed a piecewise wind speed function, which greatly expanded the application of the Dalton formula wind speed function. Teng (2011) established a correction coefficient function composed of main influencing factors to correct the primary function organized of relative secondary characteristics so that the model has better fitting accuracy. In addition, some area-specific evaporation models have been developed. For example, Chen and Mao (1995) verified a new water surface evaporative heat dissipation coefficient applicable in China through experiments. Moreover, Hong and Fu (1993) modified the Penman correction formula for China on the basis of experimental evaporation data measured in China.

WAIE models have been used in urban planning and mainly focus on the effect of water bodies on residential areas. By using a CFD model and WAIE model, Yang et al. (2015) simulated the effects of temperature, relative humidity, and wind speed changes under various building layouts in a residential area. Jiang et al. (2013) established a simple kinetic model of heat and moisture exchange between a water body and the atmosphere to investigate the effects of different water body conditions on the heat and humidity in an urban area.

To sum up, existing research provides useful insights into PM and WEAI models and their applications. The PM and WAIE models have been used in various applications in different research fields. There are, however, some gaps and shortcomings. The first problem is that the existing literature on UWA mainly focuses on theoretical aspects, for accurately simulating the effect of a water body on a complex urban 3D spatial wind environment, these models must be combined. These have often been presented in general and descriptive forms with limited discussion on real-world practical application. Second, research on the urban wind environment simulation is mainly concentrated at the whole city or the larger regional level, while on the scale of about 10km² 3D urban space, due to the lack of detailed and accurate data, despite its decisive role in wind adaptive urban planning and design, few studies have been carried out. Third, although some studies have investigated the impact of urban waterfront spaces on the urban wind environment, there is still a lack of useful information for urban planners and policy makers. Therefore, explicit research is needed to gain an in-depth understanding of the high-precision 3D impact of urban waterfront space

on the urban wind environment. As a step to fill these gaps, this paper aims to demonstrate how to integrate PM and WAEI models into the computer fluid dynamics for fine three-dimensional simulation of urban waterfront wind environments, and how to apply the integrated model to the wind environment adaptive planning and design.

3. Study area

The research area of this paper is located in the Gongshu section, the key section of the Beijing-Hangzhou Grand Canal that flows through the central area of Hangzhou. The study area is located between Liushi and Desheng expressways in the north and south, and is bounded by Shangtang Elevated Road, Tongyi Road and Moganshan Road in the east and west. The area is 7.91km², of which the water area is 0.59km² (Fig. 1).

According to the analysis of meteorological data over the years and Climate Consultant software, the average monthly temperature in the main urban area of Hangzhou is about 16.7°C, but the temperature values in January, February, August and December seriously deviate from the comfort threshold; the air humidity remains above 60% throughout the year, which was always above 70% in June. The monthly average wind speed is 2.4 m/s, the average wind speed in summer and winter is 3 m/s and 2 m/s respectively, and the maximum wind speed in most wind directions is lower than 10 m/s. 20°WSW and 40°WN are the dominant wind directions in summer and winter, respectively. It can be seen that the temperature in summer and winter in the main urban area of Hangzhou is above and below the comfort threshold, the relative humidity is high, the wind speed is low, and the wind-heat environment is poor(Supplementary Figs. 1 and 2).

4. Integration of the PM and WAIE models

4.1. Physical PM model and its simplification

When simulating an urban wind field, completely simulating all the details for an entire city is a highly time-consuming process. In the present study, groups of urban buildings were considered a porous

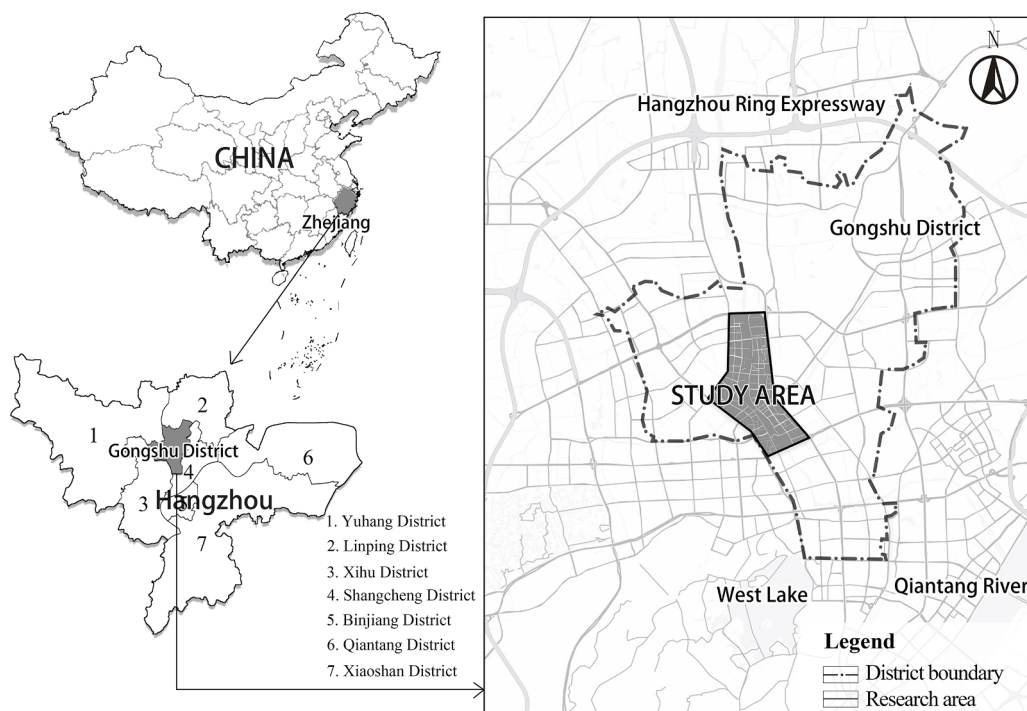


Fig. 1. The study area and its location in China and the city of Hangzhou.

medium to simplify the calculations of the PM model. The simplification of the physical PM model involved simplifying the 3D city model and simulation parameters. Because the wind environment of building groups is different from that of individual buildings, buildings with similar heights and shapes were combined into groups. The effect of a building group on the wind environment was related to the buildings' spacing and height. According to Ma's simulation of eddy currents on the street (Ma, 2006), when building spacing to building width and height (B/H and B/W) equals 0–1, a building group can be integrated into one building.

The momentum equation for PM is obtained by adding viscous and inertial losses to the standard momentum equation (Andrejko & Sidorenko, 2019). When a porous medium is isotropic, the following simplified momentum equations are obtained:

$$S_i = -\left(\frac{\mu}{\alpha}v_i + C_2 \frac{1}{2} \rho |v| v_i\right) \quad (1)$$

$$\Delta p = -S_i \Delta n \quad (2)$$

where Δp represents the pressure drop and Δn represents the thickness of the porous medium. Viscous loss, inertial loss, and porosity are indispensable parameters in the PM model. The calculation of viscous resistance and inertial resistance should be based on the experimentally measured wind speed. The pressure drop is then simulated in ANSYS Fluent by using the PM model to obtain a quadratic curve of the wind speed versus the pressure drop. When the porous medium is air, μ and ρ are equal to 1.7894×10^{-5} and 1.225 kg/m^3 , respectively. Corresponding the parameters of the quadratic curve to the viscous loss term and the inertial loss term, the viscous loss and inertial loss of the porous medium are obtained.

The porosity φ of a porous medium is the ratio of its effective pore volume to its total volume (Liu, 2009). When the wind direction is not parallel to the street, the comprehensive porosity is used to evaluate the fluid storage capacity of a porous medium. The comprehensive porosity (φ_c) is calculated as follows:

$$\varphi_c = \sqrt{\varphi_x^2 + \varphi_y^2} \quad (3)$$

where φ_x and φ_y are the porosity components in the x -axis and y -axis directions, respectively.

The porosity φ can be calculated using the following two formulas:

$$\varphi = \frac{\sum_{open_space} \pi r_{hi}^2 l_i}{\sum_{open_space} V_i + \sum_{built} V_j} \quad (4)$$

$$r_h = \frac{l h}{l + h} \quad (5)$$

where r_{hi} represents the radius of open area i of an urban canopy, l_i represents the length of open area i , V_i represents the average volume of the urban canopy, V_j represents the average building volume, r_h represents the radius of the urban canopy, l represents the average street width, and h represents the average height of the urban canopy.

4.2. WAIE model and its parameter determination

The processes of water and heat exchange between a water body and the atmosphere have considerable influences on the water body's temperature distribution, water transport, and plant growth (Dennison & Berry, 1993). These processes also play a role in regulating the local climate. A water body exchanges heat and vapor with the surrounding atmosphere, which results in changes in the temperature and humidity, respectively, of the air above the water body. During the heat and vapor exchange processes, land and water winds are generated because of the difference in the specific capacities of water and land. The heat storage capacity of water is higher than that of land, which leads to a difference

in thermal pressure between them and thus the flow of air. An irregular airflow forms around a water body when evaporation, radiation, and convection occur at the water-air interface. This information should be considered when deriving a mass or energy balance equation for studying material and energy exchange, respectively, at the water-air interface. Because the wind field around a water body is complex and variable, determining all the details of the wind field flow is impossible. Usually, in engineering and applied research, the interaction between the two is explored by establishing the relationship between the water body and the wind field.

Assuming energy conservation at the water-air interface, the heat transferred through convection can be calculated using the heat transfer of radiation and evaporation as the boundary condition for heat flow. As presented in Eq. (6), the net radiation R_n received by the water surface is equal to the sum of the sensible heat flux H , latent heat flux LE , and heat conduction flux G between the water and air.

$$R_n = H + LE + G \quad (6)$$

Material exchange at the water-air interface occurs through an evaporation process. The heat transferred during evaporation is calculated from the surface evaporation and latent heat of vaporization as follows:

$$LE = E \cdot L = E \cdot [2.501 - 0.002361 T_a] \quad (7)$$

where LE refers to the latent heat flux (W/m^2), L refers to the latent heat of vaporization (J/kg), E refers to the amount of water evaporated ($\text{kg/m}^2 \cdot \text{s}$), and T_a refers to the air temperature at a point 2 m above the water surface ($^\circ\text{C}$).

The amount of water evaporation at the water-air interface can be calculated using a water surface evaporation model. This quantity can then be used as the mass flux boundary condition for water vapor. In this study, Penman's integrated model was used to calculate the evaporation quantity with high accuracy. This model can be expressed as follows:

$$E = \frac{R_n \Delta + E_a \gamma}{\Delta + \gamma} \quad (8)$$

$$\Delta = \frac{e_a}{273 + T} \left(\frac{6463}{273 + T_a} - 3.927 \right) \quad (9)$$

$$E_a = K \left(1 + \frac{u_2}{100} \right) (e_a - e_b) \quad (10)$$

where E is the amount of water evaporation (mm/d), R_n is the net radiation received by the water body ($\text{MJ/m}^2 \cdot \text{d}$), Δ is the water vapor pressure gradient ($\text{hPa/}^\circ\text{C}$), E_a is the air dryness function (mm), e_a is the saturated water vapor pressure (hPa) when the temperature is T_a ($^\circ\text{C}$), u_2 is the wind speed at a point 2 m from the water surface (m/s), $e_a - e_b$ is the air saturation difference (hPa), and K is a constant ($K = 0.35$).

The heat transferred during the radiation process is equal to the net radiation received by the water surface, including the net solar short-wave radiation absorbed by the water surface, the sky long-wave radiation and the upward long-wave radiation on the water surface. The heat transferred in the radiation process is calculated using the following formula:

$$R_n = (1 - \alpha) S_R + L_R - \epsilon \sigma T_s^4 \quad (11)$$

where α is the heat release coefficient of the water surface ($\alpha = 0.06$), S_R is the solar short-wave radiation directly incident on the water surface (W/m^2), L_R is the amount of long-wave radiation traveling downward from the sky (W/m^2), ϵ is the long-wave emissivity of the water body ($\epsilon = 0.96$), σ is the Stefan-Boltzmann constant ($\sigma = 5.67 \times 10^{-8} \text{ W/m}^2 \cdot \text{K}^4$), and T_s is the surface temperature of the water body (K).

The net amount of solar short-wave radiation absorbed by the water surface can be calculated using the following formula:

$$S_{Rn} = (1 - \alpha)S_R \quad (12)$$

The amount of solar short-wave radiation (S_R) can be calculated to within a small error from the astronomical radiation (Kang et al., 2003) as follows:

$$S_R = (a - bs_1)Q_a \times 10^6 / t \quad (13)$$

where a and b are empirical coefficients, s_1 is the percentage of sunshine, Q_a is the amount of astronomical radiation ($\text{MJ/m}^2 \cdot \text{d}$), and t is the number of sunshine hours in a day.

Because a strong linear correlation exists between the total solar radiation and percentage of sunshine, the empirical coefficients a and b can be calculated using the least squares method. Zhang et al. (2003) fit solar radiation and sunshine percentage data obtained by the Hangzhou Observatory and calculated the empirical coefficients a and b for each

month of the year (Supplementary Table 1). In the present study, the data for July and December were used to conduct simulations for the summer and winter seasons, respectively.

The astronomical radiation Q_a can be obtained using the following formula:

$$Q_a = T \cdot I_0 (\omega_0 \sin \gamma \sin \delta + \cos \gamma \cos \delta \sin \omega_0) / (\pi \cdot \rho^2 \cdot t) \quad (14)$$

where γ is the geographic latitude, δ is the solar declination (rad), ω_0 is the hour angle (rad), ρ is the relative distance between the sun and Earth, I_0 is the solar constant ($I_0 = 13.67 \times 10^{-4} \text{ (MJ/m}^2 \cdot \text{s)}$, T is the length of a day ($T = 24 \times 60 \times 60 \text{ s}$), and t is the number of sunshine hours in a day.

The long-wave radiation emitted downward after the absorption of solar radiation by clouds can be calculated as follows as per the Stefan–Boltzmann law:



Fig. 2. Locations of the observation points, and building integration scheme in the model validation area.

$$L_R = (1 - \gamma_a) \cdot \sigma \cdot \epsilon_a \cdot (273.15 + T_a)^4 \quad (15)$$

where γ_a is the long-wave reflectance ($\gamma_a = 0.03$), ϵ_a is the long-wave emissivity of air, and T_a is the air temperature at a point 2 m above the water surface ($^{\circ}\text{C}$).

The long-wave emissivity of clear air can be calculated using the following equation:

$$\epsilon_a = 1 - 0.261 \cdot \exp(-7.77 \times 10^{-4} \cdot T_a^2) \quad (16)$$

The heat transfer flux inside a water body is small and thus was ignored in this study.

4.3. Validation of the model developed by integrating the PM and WAIE models

4.3.1. Data collection and processing

Observational data were collected to verify the accuracy of the PM and WAIE models. A relatively small area was selected for data collection. The selected area was a typical UWA that includes residential areas, commercial areas, historic locations, and plazas. The area of the study region for model validation was approximately 1.27 km², and this region included main urban roads such as Daguan Road, Dengyun Road, Lishui Road, and Jinhua South Road, secondary main roads and branch roads (Fig. 2).

A total of 14 wind speed observation points on the ground were selected (last column of Table 1). One Seema AR856a Anemometer (Shenzhen, China) anemometer was placed 1.5 m above the ground at each location for wind speed measurement. In each wind speed measurement test, data were recorded every 1 s for 10 min. In addition, three observation points were selected on the water surface at three river (Beijing-Hangzhou Grand Canal, Small River and Yuhangtang River) intersections to obtain data for calculating the material and energy exchange at the water-air interface. The measurement instruments, namely three Seema AR837 hygrometers, three Seema AS700 infrared thermometers, and three Seema AR856a anemometers, were set 0, 1.5, and 2 m above the water surface. Temperature and humidity tests lasting 1 min each were conducted at the water surface, and the data recorded by the instruments were stable. Each wind speed test lasted 3 min, with data being recorded every 10 s. The measurement times were 10:50–11:00 am on July 31, 2019, 2:00–2:10 pm and 10:50–11:00 am on December 12, 2019. The average wind speed values obtained at the 14 observation points on land and three observation points on the water surface are presented in Tables 1 and 2, respectively.

Table 1
Average wind speed at each observation location on land.

Measuring point (MP) number	Average wind speed (m/s)		Land type	Observation point type
	Summer	Winter		
MP1	0.897	0.728	City road	Along the line
MP2	1.002	0.617	Residential area	Windward side
MP3	0.988	0.775	City road	Along the line
MP4	0.565	0.619	Historic District	Windward side
MP5	0.710	0.616	Historic District	Leeward side
MP6	0.983	0.612	City road	Intersection
MP7	0.488	0.423	Square	Center
MP8	0.435	0.467	Residential area	Corner
MP9	0.544	0.474	Residential area	Windward side
MP10	0.665	0.607	Residential area	Leeward side
MP11	0.865	0.460	City road	Intersection
MP12	0.837	0.734	Commercial and business district	Corner
MP13	0.744	0.680	Commercial and business district	Leeward side
MP14	0.772	0.565	Commercial and business district	Corner

4.3.2. Partitioning of the study area and parameter calculation for the partitions

The study area was divided into eight porous partitions (Table 4) in accordance with the PM model, and an accurate model was set as the control group. The measured average wind speeds presented in Tables 2 and 3 were entered into the ANSYS Fluent software to simulate pressure drop values with real buildings in the block. After numerical fitting, the following three equations were obtained:

$$\Delta p = 0.1611v^2 + 0.0163v \quad (17)$$

$$\frac{\mu}{\alpha} \Delta n = 0.0163 \quad (18)$$

$$C_2 \frac{1}{2} \rho \Delta n = 0.1611 \quad (19)$$

By using the aforementioned equations, the viscosity coefficient, inertia coefficient, and comprehensive porosity of each block were obtained (Table 4).

4.3.3. Calculation of parameters related to water surface evaporation

Parameters related to water surface evaporation include the net solar short-wave radiation absorbed by the water surface, long-wave radiation transmitted downward from the sky, radiative heat transfer in July and December, water pressure gradient, calculated air temperature and wind speed data, dryness, evaporation quantity, and heat transfer. These parameters can be calculated using the formulas related to the WAIE presented in Section 2. The calculation results obtained for these parameters are presented in Table 5.

4.3.4. CFD simulation parameter settings

The PM and WAIE models were integrated into CFD through two steps. The first step involved determining the computational region and mesh size, and the second step involved setting boundary and solution conditions. In the CFD model developed in this study, the area of the fluid was employed. Usually, in this model, the length of the air inlet in the calculation area is approximately 3–4 times the height of a building, the length of the air outlet is 8–10 times the height of the highest building, and the calculated height is 2–4 times the height of the considered building. The computational mesh size selected in this study was 2500 m × 2100 m × 240 m (Fig. 5).

Meshing is an essential step in CFD simulations. The aim of meshing is to discretize a CFD model and decompose the solution domain into an appropriate number of elements to ensure that refined solutions are obtained. Mesh quality directly affects the accuracy of the simulation and the stability and convergence of the simulation process. In this study, the Mesh tool of ANSYS Workbench 16.0 was used for meshing. Triangular meshes were used for meshing in accordance with the geometry of the examined block and building group, and the grid size was 1–2 m.

In addition, accurate simulation results are obtained when the boundary conditions in ANSYS Fluent are set appropriately. Typically, the average wind speed at the air inlet is set as a boundary condition. Because of the different frictional forces caused by the surface morphology at different heights, a vertical wind speed distribution profile is formed, and this profile is generally logarithmic and exponential. Considering the measured wind speed values and the average wind speed profile in the horizontal direction, velocity inlet is expressed using an exponential law as follows:

$$\frac{U_i}{U_{\infty}} = \left[\frac{Z_i}{Z_{\infty}} \right]^{\alpha} \quad (20)$$

where U_i and U_{∞} are the average wind speeds at Z_i and Z_{∞} , respectively, where Z_i is the height of any location and Z_{∞} is the height of the atmospheric boundary layer in uniform flow. Moreover, α is the surface roughness factor. The surface roughness of different landforms is

Table 2

Temperature, humidity, and average wind speed data for each observation point on the water surface.

Measuring point (MP*) number	Water surface temperature (°C)		Humidity (1.5m)		Humidity (2m)		Temperature (1.5m)		Temperature (2m)		Average wind speed (m/s)	
	S	W	S	W	S	W	S	W	S	W	S	W
MP*1	31.7	6.4	34.2	53.1	30.2	51.6	37.6	11.3	38	11.7	0.533	0.460
MP*2	31.5	7.8	37.7	54.1	37.6	53.5	39.1	11.7	38.5	12.4	0.545	0.336
MP*3	31.8	8.3	41.8	51.4	40.3	50.9	36.3	12.9	36.4	12.9	0.885	0.982
Average	31.7	7.5	37.9	52.9	36	52	37.7	11.9	37.6	12.3	0.654	0.593

Table 3

Wind inflow speed for the experimental block.

Inlet	MP1 (m/s)	MP2 (m/s)	MP3 (m/s)	MP4 (m/s)	MP5 (m/s)	Average wind speed (m/s)	Wind direction
Summer	0.684	0.701	1.063	0.796	0.504	0.750	SE
Winter	0.393	0.668	0.670	0.651	0.569	0.590	SE

Table 4Scope and main functions of the eight porous partitions, viscosity loss ($1/\alpha$), inertial loss (C_2), and comprehensive porosity (φ_c) of each block in the study area.

Porous area number	The main function	Boundary range (annular area)	$\frac{1}{\alpha}$	C_2	φ_c
1	Residence	Dengyun Road, Canal, Xiaohe Road, Xiaohe river, Heyuan Lane	44.22	0.0127	0.75
2	Commerce (Historic District)	Xiaohe branch road, canal, Xiaohe river, Xiaohe road	37.80	0.0109	0.58
3	Commerce (Historic District)	Xiaohe River, Xiaohe Road, Hemu Road, Guyun Road	39.95	0.0115	0.42
4	Residence	Hemu Road, Guyun Road, Zhaowu Road, Xiaohe River	34.12	0.0098	0.76
5	Residential area	Hemu Road, Xiaohe Road, Hushu North Road, Cannel, Zhaowu Road, Guyun Road	34.90	0.0100	0.69
6	Residence	Hushu North Road, Daguan Road, Zhaowu Road, Yuhangtang River	26.48	0.0076	0.77
7	Residence	Jinhong Street, Jinhua South Road, Dahu Street, Lishui Road	29.96	0.0086	0.68
8	Residence, business office	Dahu Street, Shangtang Road, Daguan Road, Jinhua Road, Yuanjian Street, Lishui Road	24.69	0.0071	0.77

Table 5

Calculation results for the radiation parameters, net radiation received by the water surface, and evaporation parameters.

Parameter	July	December
Astronomical radiation (Q_a , MJ/(m ² ·d))	38.6730	19.6793
The amount of solar shortwave radiation (S_R , W/m ²)	520.6943	492.1721
Net amount of solar shortwave radiation absorbed by the water surface (S_{Rn} , W/m ²)	489.4526	462.6418
Sky longwave radiation (L_R , W/m ²)	468.2363	280.4180
Net radiation received by the water surface (R_n , W/m ²)	450.1155	381.6712
Water pressure gradient (Δ , hPa/°C)	36.9488	8.5089
Air dryness (E_a , mm)	9.8069	1.6936
Evaporation (E , mm/d)	14.7506	3.9721
Heat transfer during evaporation (LE , W/m ²)	411.8254	113.6430

different. According to the Chinese standard, α was set as 0.3 in the present study. For the selected surface roughness, Eq. (20) was revised as follows:

$$U = 0.357 U_i Z^{0.3} \quad (21)$$

where U_i is the measured average wind speed, and Z is the average height of the study area.

Given that the air inlet speed was not constant, the inlet_velocity.c entry subroutine had to be written and imported into the main CFD program (Supplementary 1). A water vapor diffusion boundary inlet was set at the water vapor interface as per the PM model. The amount of evaporation was used as the boundary condition for the water vapor mass flux. Moreover, the water vapor mass fraction (m) was used as the water vapor diffusion index. The water vapor mass fraction can be calculated from the air moisture content, see Eq. (22).

$$m = \frac{d}{1+d} \quad (22)$$

where m is the water vapor mass fraction, and d is the air moisture content (g/kg). The calculated air moisture content (d , g/kg) in July and December was 1.56 and 0.45, respectively, and the water vapor mass fraction (m) was 0.6094 and 0.3103, respectively. The simulated outlet boundary condition could be set to Pressure-outlet with a relative pressure of 0. Under this condition, the air reaching the outflow face was assumed to develop sufficiently; that is, the outflow face's air flow was unobstructed by any structure. Moreover, symmetry is used for top and turbulent boundaries; walls are used for building surfaces and ground. The adopted simulation scheme includes the following parameters: the model of, the control method used in, the supervisory control method used in, and the number of iterations in the simulation scheme. The renormalized group $k-\epsilon$ model was used, and C_{mp} , C_1 , and C_2 were set to the software default values, namely 0.0845, 1.42, and 1.68, respectively. The SIMPLE algorithm was used to decouple pressure and velocity to avoid unreasonable pressure and velocity values. The near-wall region was processed using the wall function method. The criteria for convergence were that the residual curve was flat and that the residual values for all variables were smaller than 10^{-3} .

4.3.5. Comparison of the simulation results and measurement data

The simulated wind speeds in summer and winter for the study area are displayed in Fig. 3. These results indicate that the wind speed distribution in the study area was similar in summer and winter, with the wind speed in summer being marginally higher than that in winter. The simulated cloud map indicates that the wind speed at a height of 1.5 m above the water surface was lower than that at the surrounding buildings. However, the horizontal wind speed around the water body increased considerably. Moreover, the horizontal wind speed around the

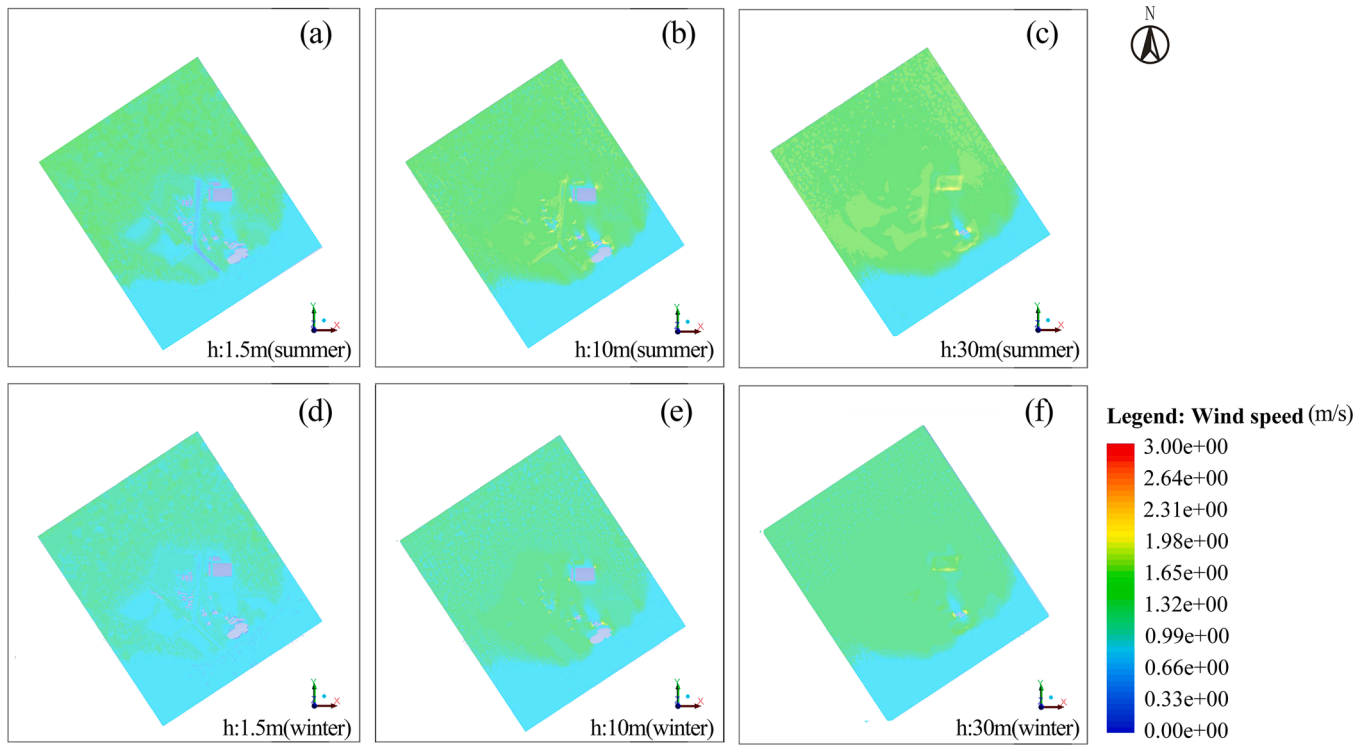


Fig. 3. Cloud map of the simulated wind speed in summer and winter in the model validation area.

water body remained high at elevations of 10 and 30 m above the water surface, especially in summer. For example, the wind speed in the downwind direction of Sanjiangkou was approximately 0.3–0.5 m/s higher than that in the surrounding areas. Porous regions 4, 5, and 7 were thick in the inflow direction of the wind and had a relatively strong blocking effect on the wind. The two large buildings in the study area, namely Ocean Ledi Port and Silk Link 166 Creative Industry Park, were the most prominent obstacles to the wind, and their leeward side had a larger area of calm wind than did their windward side.

The correlation coefficient (R^2) was used to determine the degree of fit between the simulation and measurement data. The closer R^2 was to 1, the better was the fit. The parameter R^2 is expressed as follows:

$$R^2 = \frac{[\sum_i(y_i - \bar{y})(\hat{y}_i - \hat{\bar{y}})]^2}{[\sum_i(y_i - \bar{y})^2][\sum_i(\hat{y}_i - \hat{\bar{y}})^2]} \quad (23)$$

where \bar{y} is the measured average wind speed, \hat{y} is the wind speed obtained through simulation based on the PM model, and $\hat{\bar{y}}$ is the average wind speed obtained through simulation based on the PM model.

R^2 was higher than 0.7 for the simulations based on the PM model and the buildings in the study area; thus, the data obtained in both simulations fit the measured data well. The difference in R^2 between the simulations based on the PM model and the buildings in the study area was 0.044 and 0.042 for summer and winter, respectively, with the simulation based on the buildings in the study area being marginally more accurate. However, the average simulation time when considering the buildings in the study area was approximately twice that when using the PM model; thus, the simplified PM model saved considerable computational time (Table 6).

5. Methodology and results: application of the developed integrated model to a case study

The integrated model developed in this study was applied to a UWA with an area of approximately 7.91 km². Moreover, the results obtained with this model were used as a basis to design strategies for the planning

Table 6
Error and calculation time for the two adopted simulation methods.

Simulation method	Error from measured results (R^2)	Number of iterations	Average simulation time
Porous Media Simulation	Summer 0.714 Winter 0.702	500	6:09:35
Real Building Simulation	Summer 0.758 Winter 0.744	500	12:12:19

of wind environments in urban design. The two goals of wind adaptation planning and design are to promote wind flow in the simulated area and to achieve pedestrian comfort. Therefore, these factors need to be considered when formulating wind environment design strategies based on numerical simulation results (Fig. 4).

5.1. Characteristics of the selected simulation area

The selected simulation area was expanded on the basis of including the area where the observation points were located (Fig. 1). Fig. 5a presents the land use pattern of the selected area. The total land area was 7.91 km², of which urban construction land accounted for 7.32 km² and water accounted for 0.59 km² (Supplementary Table 2).

Overall, the intensity of construction in the study area was higher in the south than in the north. The construction intensity on both sides of the canal to the north of Desheng Expressway was relatively low. This area mainly included large-scale riverside green spaces with residential and commercial buildings that were constructed many years ago. Residential land occupies nearly half of the urban space in the simulation area, and the building layout in the residential area is very regular. The low-rise residential area in the simulation area consisted of 1–3-story courtyards, which were arranged in a straight line. Most multistory residential complexes were 4–6-story townhouses arranged in a regular pattern. The high-rise residential areas included buildings with 9–12 stories and more than 18 stories. Except for some historic areas, most of

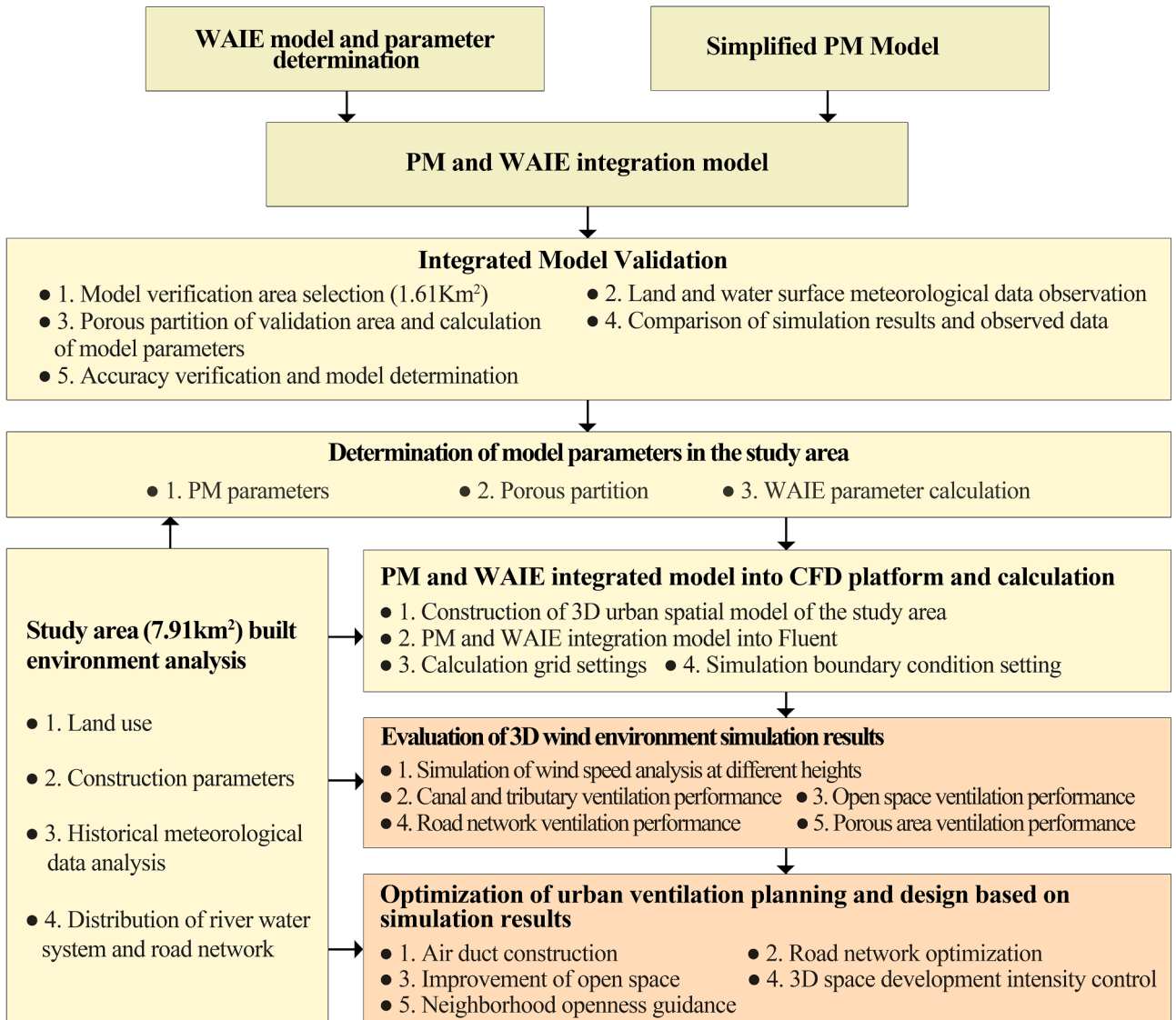


Fig. 4. Technical process of applying the developed integrated model.

the residential areas in the simulation area were constructed after 1970. More than 60% of the residential areas were constructed after 2000. The type of residential area had a strong correlation with the age of construction. Most of the buildings constructed from 1980 to 2000 were multistory buildings and inhabited by the Chaochongshengli and Chongqingli communities. High-rise residential areas and multistory mixed high-rise residential areas were developed after 1995, mainly in the areas north of Daguan Road and west of the canal. The low-rise residences in the simulation area primarily included buildings in historical areas and high-end villas constructed after 2010. The building density, building height, and plot ratio reflected the construction intensity of a plot to a certain extent (Supplementary Table 3).

From the perspective of air channel planning elements, river channels, as urban open spaces, are a crucial part of urban ventilation corridors (UVCs) (Wang et al., 2022). The river channel in the simulation area was the main wind circulation path in this area and thus should be the focus of wind environment optimization. From Liushi Expressway in the north to Desheng Expressway in the south, the river channel had a width of approximately 50–120 m. Through the internal tributaries of Yuhangtang River, Nanyingjia River, Shangtang River, Yaojiaba River and other arms to guide the flow of wind to the block, the river surface width of the tributaries is about 10–30 m.

Buildings and roads are the basic spatial texture features of a city. Urban road networks are crucial networks of urban air circulation, and the geometry, direction, width, and layout of urban road networks affect the urban wind field and airflow (Golany, 1996). The main roads in the simulation area were Tongtong Road, Dengyun Road, Moganshan Road, the Shangtang Elevated Road, the Liushi Expressway, Daguan Road, and the Desheng Expressway. The secondary roads in this area included Xiao Road and Lishui Road. The branch roads in the area included Hedong Road and Sheng Lane. In addition, alleys with a width of mostly less than 5 m were present in historical areas, urban villages, and other areas. The overall road network density in the study area was relatively high (i.e., 10.08 km/km²). The main road network had a relatively complete and balanced layout. The density of the secondary road network was low, with this density being higher in the west and north than in the east and south, respectively. The branch road network was unevenly distributed and contained many open paths, which are not conducive to the circulation of wind in areas with high building density.

5.2. Simulation of the ventilation potential, calculation of parameters, and setting of boundaries

By using the building merging method described in Section 2, the

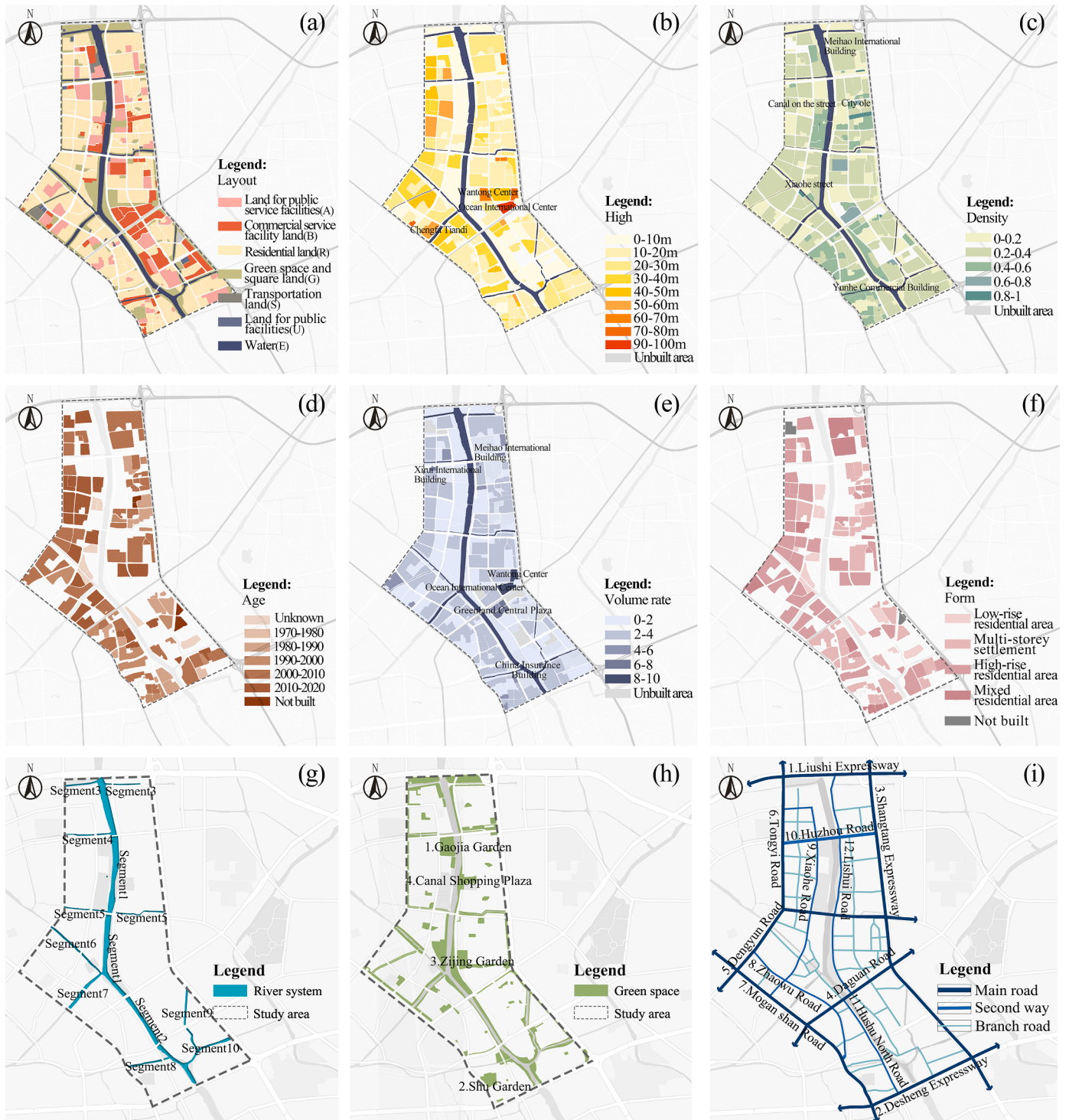


Fig. 5. Analysis of current land use, buildings, rivers, roads and greening in the simulated area.

study area was divided into 18 blocks as PM (Fig. 6). The length and height of the air inlet and outlet in the calculation area were the same as those mentioned in Section 2. The size of the calculation area in the simulation was $5600 \text{ m} \times 4200 \text{ m} \times 240 \text{ m}$. When the residual value of all variables was less than 10^{-3} , the residual curve was flat. The viscosity coefficient ($1/\alpha$), coefficient of inertia (C_2), and comprehensive porosity of each block were calculated using the method described in Section 2 (Table 11).

The channel evaporation parameters and water vapor mass fractions, which were calculated using the method described in Section 2, were

used as the water vapor inlet boundary conditions and diffusion conditions, respectively (Table 7).

5.3. Evaluation of the simulation results

5.3.1. Simulated wind speed at different heights

In summer, the wind speed in the study area was primarily 0.5–3.3 m/s at a height of 1.5 m, with the highest and lowest wind speeds being 4.4 and 0.08 m/s, respectively. Combined with the “comfortable” range of wind speed proposed by different scholars, the pedestrian height

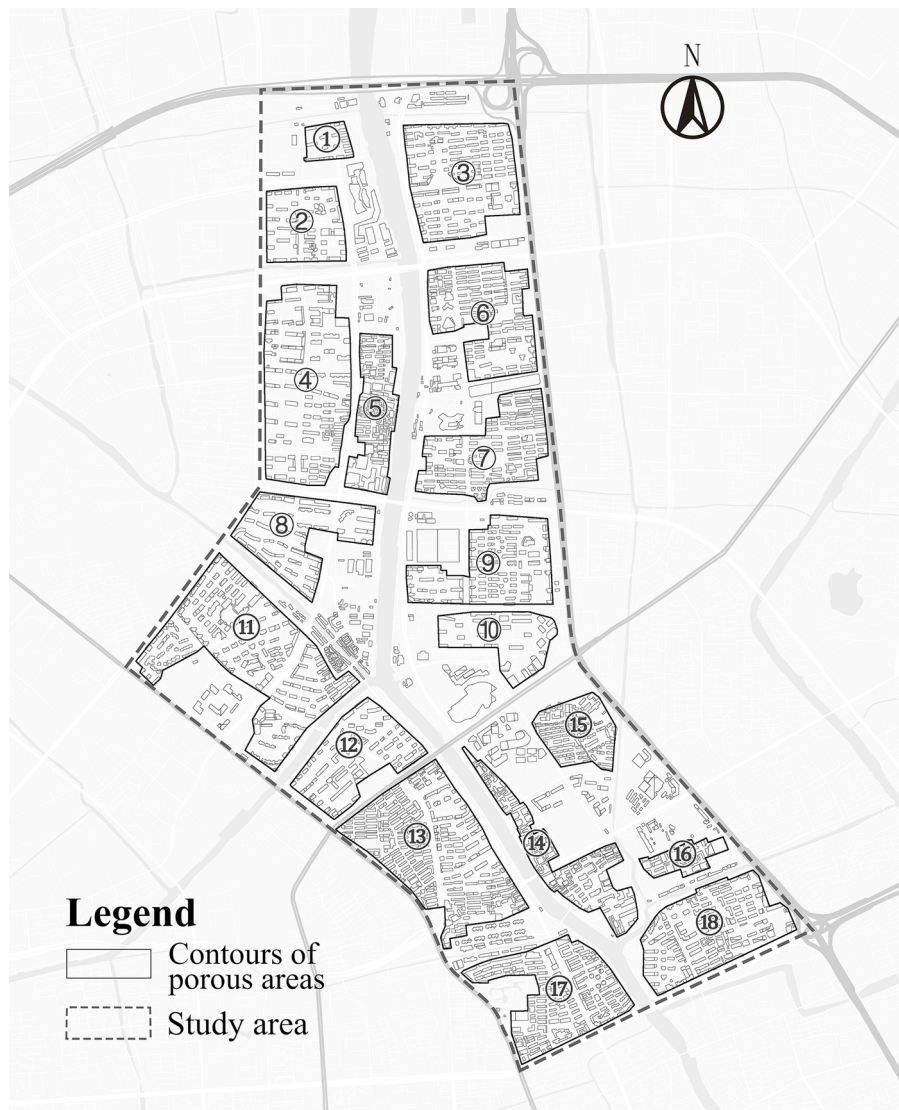


Fig. 6. Division and numbering of porous media blocks in simulation area.

Table 7

Parameters related to water vapor diffusion.

Parameter	July	December
Evaporation (E , mm/d)	14.7506	3.9721
Heat transfer during evaporation (LE, W/m ²)	411.8254	113.6430
Water vapor mass fraction (m)	0.6094	0.3103

comfort target constraint range of wind speed in summer is 1–5 m/s, and the comfort target constraint range of wind speed in winter is 0.8–2 m/s (Simiu & Scanlan, 1992). A total of 20% of the wind speeds in the study area lay in the range of comfortable wind speeds for pedestrians. The spatial distribution of simulated wind speeds in the study area was lower in the south and higher in the north, more down in the west and higher in the east. Because the wind inflow direction was 20° southwest in summer and the intersection angle with the canal was enormous, so the ventilation effect of the canal was not obvious at the height of 1.5m; therefore, the wind speed was low (0.27–1.08 m/s), and the level of pedestrian comfort was poor. However, high wind speeds occurred in the clearance between the tall buildings in the simulation area. High inner wind speeds were discovered in areas 2, 3, and 4, which had the highest porosity. The average and maximum wind speeds in these areas were 2.4 and 3.2 m/s, respectively, and these areas had high pedestrian

comfort. Areas 5, 6, and 13–18 had low porosity and wind speeds of 0.9–1.2 m/s but were comfortable for pedestrians. However, areas with wind speeds below 0.5 m/s accounted for most of the simulation area, and these areas had poor pedestrian comfort (Fig. 7a and d).

The area with low wind speed on the east bank of the canal was considerably smaller at a height of 10 m than at a height of 1.5 m. 10m is the middle height of multi-storey buildings common in Chinese cities, and 30m is the middle height of high-rise buildings. At the height of 10 m, the area above only appears in the area north of the confluence of the canal, Xiaohe and Yuhangtang River. Between Greenland Central Plaza and Jinlan Apartment, the narrow tube effect emerged between the high-rise buildings. The wind speed was much higher at more than 4.3 m/s between these buildings (Fig. 7b and e). At a height of 30 m, the summer wind speed in the simulation area was generally above 3 m/s, with the maximum wind speed being 5.5 m/s. Because almost no high-rise buildings existed on the canal's west bank, 70% of this area had wind speeds above 4.5 m/s (Fig. 7c and f), which indicates that the tube effect was weak in this area. The wind speed between high-rise buildings distributed parallel to the wind inflow direction was higher than 5 m/s; thus, areas with such buildings are favorable for regional ventilation.

5.3.2. Ventilation performance of the canal and its tributaries

The wind speed in the canal at a height of 1.5 m was mainly affected

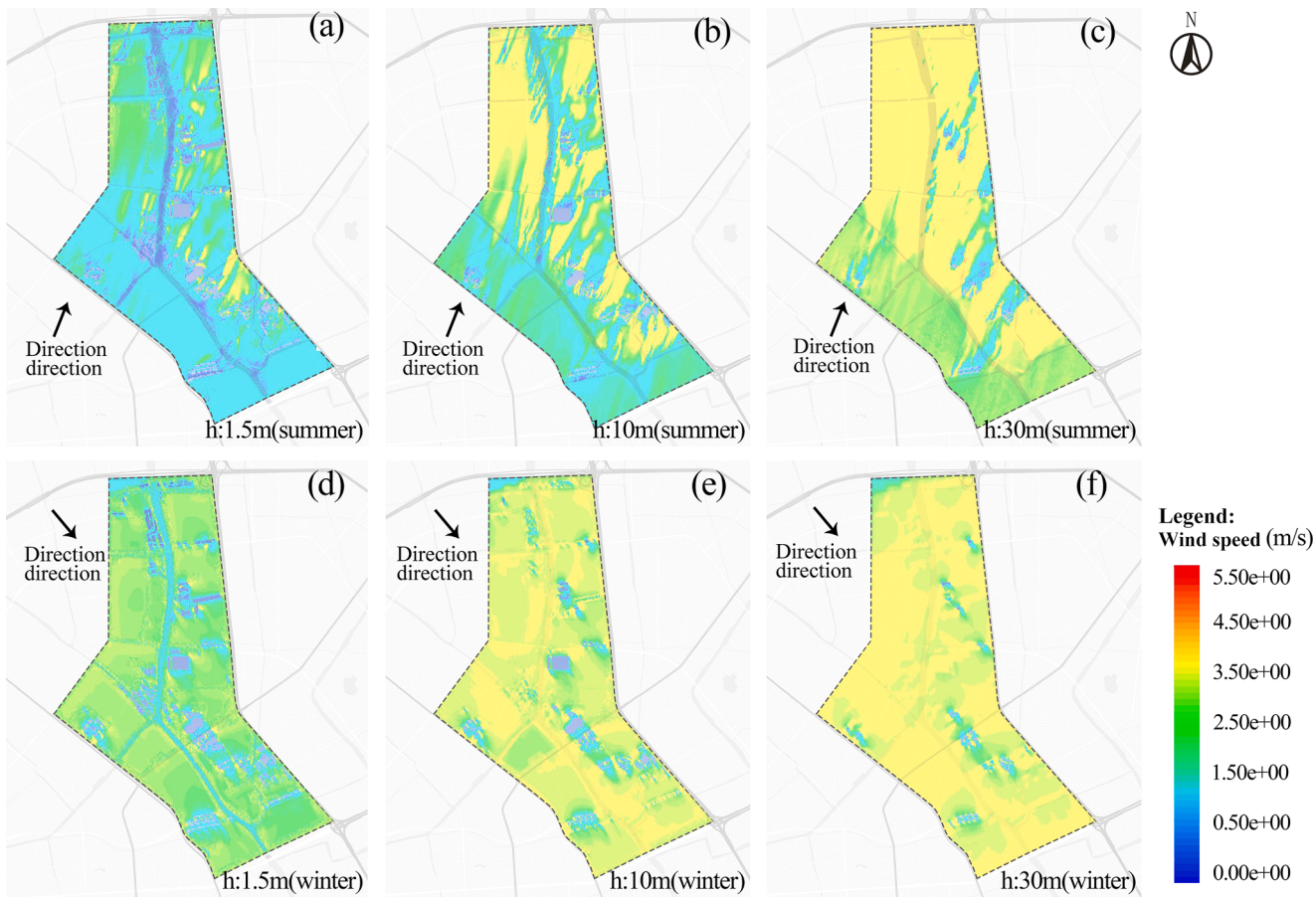


Fig. 7. Simulated cloud maps of the wind speed at heights of 1.5, 10, and 30 m in summer and winter in the simulation area.

by the surrounding buildings and was apparently uncorrelated with the characteristics of the canal (Fig. 5g). In summer, the wind speeds at heights of 10 and 30 m were significantly correlated with the width of the channel and the angle of intersection with the direction of water flow. The wind speed in a tributary was strongly affected by the lateral airflow between buildings and the narrow tube effect but not by the tributary characteristics. In winter, the wind speeds at heights of 10 and 30 m were strongly correlated with the river's intersection angle with the incoming water flow but weakly correlated with the channel width. For example, the wind flow in segment 8 was blocked by buildings; therefore, the average wind speed in this segment was 0.2–0.4 m/s lower than that in other tributary segments (Table 8).

5.3.3. Ventilation performance of the road networks

The simulation results indicate that the primary and secondary arterial roads generally had high ventilation potential (Table 9). At a height of 1.5 m, the wind speed was positively correlated with the road width. Moreover, the presence of green belts around roads was found to considerably increase the thickness of ventilation corridors. For example, the Liushi Expressway and Shangtang Road are very wide, and green belts exist on both sides of these roads. These belts were discovered to form ventilation corridors with a width higher than 70 m; thus, the simulated wind speed around these roads was very high. Although the Desheng Expressway has a width of 30–50 m, it has no green belt and is close to buildings, meaning that its ventilation performance was relatively poor. The wind speed was also related to the wind direction. For example, Daguan Road and Dengyun Road have a width of 30 m and

Table 8
Simulated wind speeds in different canal sections.

Subparagraph type	Subparagraph number	Subparagraph parameter	Summer			Winter					
			L(m)	W(m)	$\alpha(^{\circ})$	V (m/s)	1.5 m	10 m			
Main stream	1	2900	70-120	15-30	0.433	2.233	3.416	75-90	1.664	2.422	3.195
	2	2100	50-60	65-70	0.756	2.139	2.992	5-10	1.376	2.757	3.238
Tributary flow	3	1100	15-25	62-64	1.099	2.747	4.230	56-58	1.886	2.688	3.209
	4	686	8-20	69-70	2.072	3.265	4.230	50-51	2.230	2.663	2.936
	5	1500	5-15	70-78	1.146	2.800	3.928	37-45	2.250	2.749	3.223
	6	1000	11-32	78-82	0.602	1.781	2.894	38-42	1.980	2.592	3.152
	7	682	30-50	24-34	0.424	1.678	2.926	84-86	2.086	2.568	3.125
	8	644	5-20	55-65	0.754	1.694	2.806	55-65	2.206	2.368	2.898
	9	959	5-20	15-55	0.803	2.532	3.224	65-75	2.089	2.687	3.247
	10	793	13-30	42-48	0.856	1.972	3.173	72-78	1.918	2.663	3.33

Note: L stands for length; W stands for width; α stands for intersection angle with incoming flow; V stands for average simulated wind speed.

Table 9

Simulated wind speeds around the main roads in the simulation area.

Road grade	Road name	W(m)	G	Summer					Winter				
				α (°)	V (m/s)			α (°)	V (m/s)				
					1.5 m	10 m	30 m		1.5 m	10 m	30 m		
Main road	Liushi Expressway	50-70	Y	65-68	2.064	3.136	4.390	52-55	2.447	2.399	3.183		
	Dengyun Road	30	Y	73-75	1.746	2.980	3.760	45-47	2.396	2.815	3.230		
	Daguan Road	30	P	35	2.376	2.716	3.312	85	1.992	2.399	3.055		
	Desheng Expressway	30-50	N	44	2.056	2.360	2.993	76	2.375	2.784	3.180		
	Tongyi Road	25	P	19/18	1.914	2.848	2.800	12/49	2.496	2.664	3.112		
	Moganshan Road	25	P	50-72	2.152	2.452	2.930	2-20	2.418	2.735	3.213		
	Shangtang Road	30-40	P	26/63	2.462	3.066	3.342	44/7	2.184	2.672	3.168		
	Huzhou Street	15	Y	63	2.088	2.836	4.133	57	2.464	2.656	3.143		
Secondary road	Xiaohu Road	15-20	N	15-25	2.110	2.834	3.726	50-85	2.432	2.543	3.183		
	Zhao Wulu	20	N	20-80	1.910	2.336	2.762	10-50	2.352	2.640	3.185		
	Hushu North Road	15	Y	44-47	1.668	2.364	2.872	23-26	2.375	2.683	3.178		
	Lishui Road	15	Y	15-40	1.804	2.142	3.312	20-55	2.592	2.745	3.134		

Note: W stands for road width; G stands for green belt on both sides; Y stands for yes; N stands for no; P stands for partial yes; α stands for intersection angle with incoming flow (°); V stands for average simulated wind speed.

have green belts on both sides. The difference in wind speeds around these roads at a height of 1.5 m was mainly caused by the different wind direction angles around these roads. In winter, the highest wind direction angle was observed at Daguan Road, where the lowest average wind speed occurred at a height of 1.5 m. At the height of 10m and 30m, due to the abrupt disappearance of the building space, the width and direction of the road have nothing to do with its characteristics, so the wind speed distribution also presents uncertainty.

5.3.4. Ventilation performance of open spaces

The ventilation of large open spaces with a point-like distribution was examined (Fig. 5h). According to the simulation results (Table 10), the wind speed of open spaces was not clearly correlated with the area of the spaces but was strongly affected by the spaces' location. The wind speed at the height of 10m and 20m in parks and squares by the river is significantly higher than that not by the river.

5.3.5. Ventilation performance of porous areas

The simulated wind speed in a porous region is closely related to the region's porosity. For example, at a height of 1.5 m, when the porosity of a porous zone was higher than 0.7, the average summer wind speed was higher than 2 m/s. A similar finding was discovered at a height of 10 m; however, at a height of 30 m, because the thickness of most of the porous areas was less than 30 m, the porosity did not have a major effect on the wind speed. The simulated wind speeds in different porous areas are presented in Table 11.

5.3.6. Comprehensive comparison of the wind speed in different spaces

In summer, at a height of 1.5 m, roads exhibited the best ventilation performance, followed by point-shaped open spaces, porous areas, and the river channel (Table 12). The wind speed of the river channel is generally lower than that of other spaces. This result was obtained because the elevation of the horizontal plane was lower than that of the ground and because the wind inflow was not only affected by buildings,

plants, and structures on the ground but also blocked by the river bank. Surface turbulence was found to mainly originate from evaporation of water from the river channel. However, in summer, the surface temperature of the river is 7°–10° lower than the surrounding air temperature, which results in cold air flowing into urban spaces.

5.4. Optimization of ventilation design on the basis of the simulation results

5.4.1. Combining canals, roads, and open spaces to construct a two-level UVC

According to the simulated wind speeds for winter and summer and the building composition in the simulation area, four secondary ventilation corridors were designed to improve wind circulation in the area and the ventilation ability of the canal as the primary ventilation corridor (Fig. 8c). The simulation results indicate that in summer, the river channel forms an area with low wind speeds at a height of 1.5 m. Moreover, the ventilation performance of the channel is poor at heights of 10 and 30 m. However, in summer, the temperature of the canal area is considerably lower than that of the surrounding area, which indicates that the temperature of the urban space can be effectively reduced by directing the wind to flow through the canal area. Therefore, measures should be taken to enhance the ventilation effect of the canal as the main UVC. The building height of the blocks around the canal can be controlled according to the distance gradient so that the main UVC width is guaranteed to be 150–200m. At the same time, four secondary UVCs were constructed based on tributaries and trunk roads. The intersection angle with the dominant wind direction was less than 30°, and the width was maintained at 40–50m. The primary role is to communicate the main airway with the city block and as a supplement to the main UVC. When the urban road layout is designed by considering the prevailing wind direction, the ventilation capacity inside the simulation area can be considerably increased.

Table 10

Simulated wind speed in open spaces.

Name	Area (hm ²)	R	Summer			Winter		
			V (m/s)			V (m/s)		
			1.5 m	10 m	30 m	1.5 m	10 m	30 m
Gaojia Garden	6.06	Y	1.908	2.515	4.145	2.012	2.673	3.173
Canal Shopping Plaza	2.89	Y	1.811	2.866	4.221	1.915	2.681	3.261
Bauhinia Park	3.16	N	2.26	2.641	2.923	2.148	2.492	3.070
Villa Garden	3.60	N	1.51	1.986	2.712	2.137	2.684	3.220

Note: R stands for 'Whether by the river or not'; Y stands for Yes; N stands for No; V stands for average simulated wind speed.

Table 11

Simulated wind speeds in porous areas.

Porous area serial number	$\frac{1}{\alpha}$	C_2	φ_c	high (m)	Summer			Winner		
					V (m/s)			V (m/s)		
					1.5 m	10 m	30 m	1.5 m	10 m	30 m
1	46.29	0.0133	0.74	29.25	2.243	3.058	4.07	2.111	2.588	3.038
2	21.64	0.0062	0.75	36.19	2.108	3.244	4.09	2.288	2.492	3.052
3	13.83	0.0039	0.73	23.39	2.198	3.230	4.070	2.403	2.443	3.131
4	12.49	0.0036	0.77	25.33	2.352	3.012	4.370	2.396	2.602	3.140
5	24.49	0.0070	0.50	6.34	1.844	3.396	3.860	2.250	2.683	3.133
6	14.59	0.0042	0.66	16.74	1.582	2.472	3.530	2.388	2.635	3.048
7	18.16	0.0052	0.71	16.96	2.458	2.496	3.740	2.003	2.252	2.989
8	15.86	0.0045	0.75	24.91	1.932	2.694	3.722	2.446	2.575	3.125
9	20.86	0.0060	0.72	22.99	1.798	2.448	3.040	2.300	2.393	3.022
10	26.43	0.0076	0.76	62.00	2.040	2.492	2.826	2.266	2.592	3.130
11	9.39	0.0027	0.75	29.36	1.624	1.878	2.770	2.463	2.673	3.112
12	22.37	0.0064	0.77	31.80	1.756	2.294	2.798	2.444	2.397	3.135
13	10.45	0.0030	0.67	16.73	1.516	2.032	2.798	2.323	2.593	3.117
14	21.24	0.0061	0.55	7.51	0.678	2.336	2.690	2.223	2.680	3.118
15	27.43	0.0079	0.64	11.58	2.266	3.056	3.682	2.349	2.583	3.109
16	58.46	0.0168	0.43	8.53	1.644	2.890	3.658	2.251	2.540	3.045
17	17.88	0.0051	0.64	18.03	1.396	2.084	2.690	2.148	2.395	3.115
18	23.55	0.0068	0.69	20.00	1.462	2.26	2.878	2.103	2.683	3.101

Note: $\frac{1}{\alpha}$ stands for the viscosity coefficient; C_2 stands for the inertia coefficient; φ_c is the comprehensive porosity; V is the average simulated wind speed.

Table 12
Simulated average wind speeds in different types of spaces.

Space type	Summer			Winner		
	Average simulated wind speed (m/s)			Average simulated wind speed (m/s)		
	1.5 m	10 m	30 m	1.5 m	10 m	30 m
River	0.895	2.284	3.382	1.968	2.615	3.155
Roads	2.029	2.723	3.361	2.376	2.644	3.163
Open Spaces	1.872	2.502	3.499	2.053	2.632	3.180
Porous Area	1.833	2.632	3.405	2.286	2.544	3.092

5.4.2. Optimization of the road network structure for improving ventilation

Because of the uneven distribution of water bodies and buildings along the road network in the simulation area, optimizing the road network for enhancing its ventilation potential is difficult. First, the integrity and hierarchy of the road network should be ensured as much as possible, and the roads should have a wind direction angle of less than 30° in summer for smooth ventilation. Second, there should not be too many roads across the canal, and the directions of the roads on the east

and west sides of the canal should be integrated to provide space for wind flow. Finally, green space should be reserved on both sides of the UVC on the central road to increase the width of the air duct (Fig. 8b).

5.4.3. Improving the open space system by supplementing the ecological functions of the canal

Two-level wind circulation should be achieved (Fig. 9). First, the large parks and open spaces at the end of the water system should be connected by continuous linear spaces to form a low-temperature ventilation corridor in summer and achieve a suitable landscape effect. Second, positive urban exterior spaces, such as crucial outdoor commercial streets and public service centers, cannot be ignored in ventilation design.

5.4.4. Adoption of a reasonable development intensity and layout for high-rise buildings to promote regional ventilation

This study found that, at heights of 10m and above, regional ventilation was less correlated with road and river layout but strongly correlated with how tall buildings were arranged. High-rise buildings should be constructed such that they are parallel and perpendicular to the wind flow direction in summer and winter, respectively (Fig. 8a).

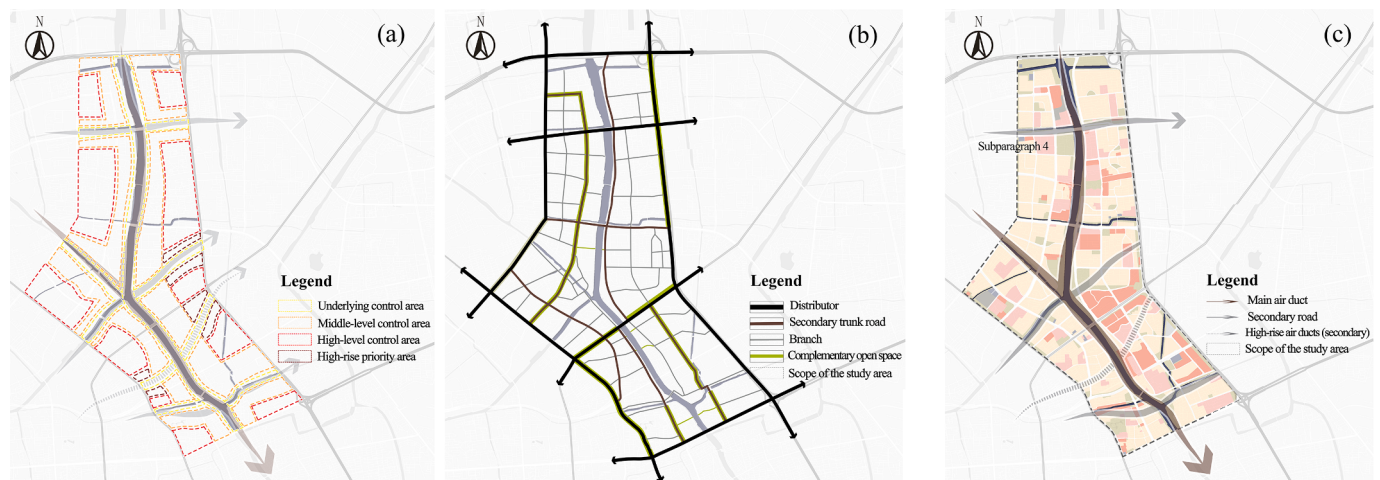


Fig. 8. Ventilation design for the simulation area.

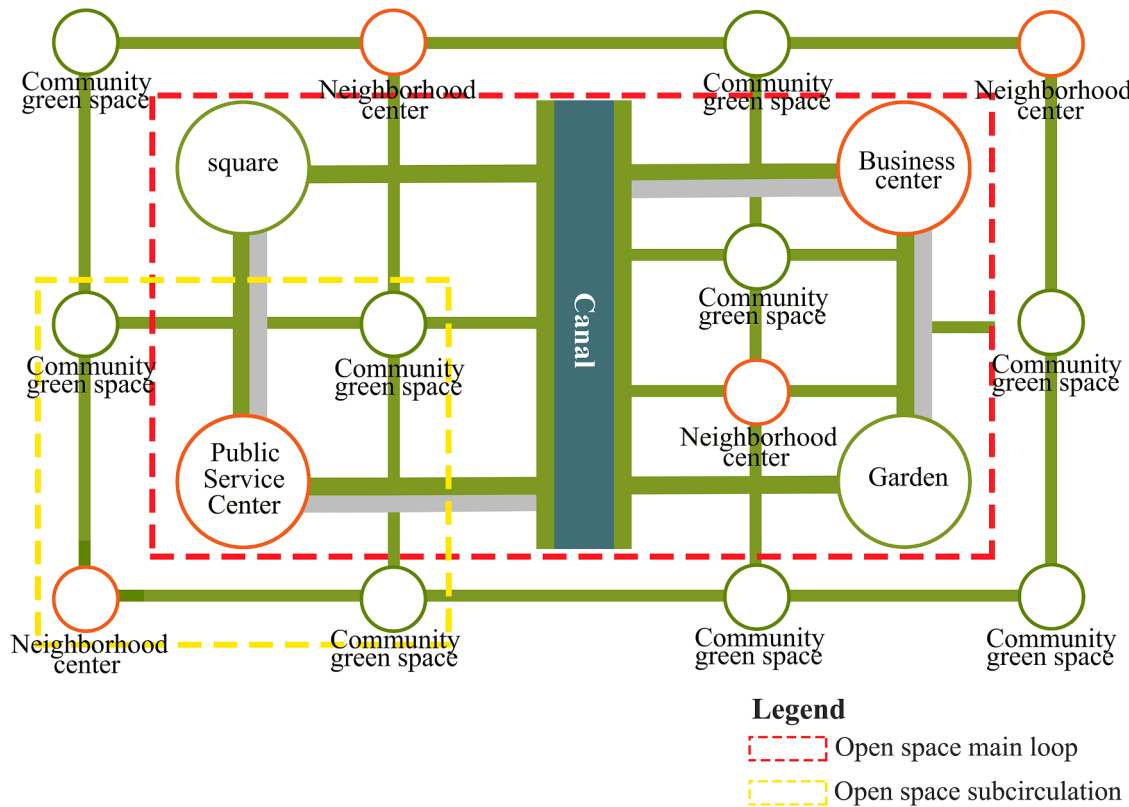


Fig. 9. Schematic of the two-level ventilation corridor system, road network, building height, and two-stage air circulation in open spaces in the simulation area.

5.4.5. Scientific guidance on block openness and architectural control

Open plots can minimize the wind resistance of buildings, which is conducive for ventilation (Fig. 10). The newly constructed plots in the study area—such as the plots enclosed by Shangtang Road, Xiangjisi Road Tunnel, and Yuhangtang River—thus contain large open spaces and old 2–3-story buildings that must be renovated. Redesigning available plots for enhancing ventilation is a good idea. Therefore, for the reconstruction of existing blocks, the rebuilding of the podiums of the outer contour of the block is the primary method, supplemented by the

optimization of the green space system. In summer, the number and height of podiums in the wind direction, especially on the west side of the canal, should be reduced to ensure that incoming wind flows into the channel as smoothly as possible. In winter, podiums and some other structures can be arranged perpendicular to the wind flow direction to block cold winds. Moreover, strengthening the connection between open spaces, such as green spaces inside and outside a block, is essential for improving the comfort of the wind environment in the study area.

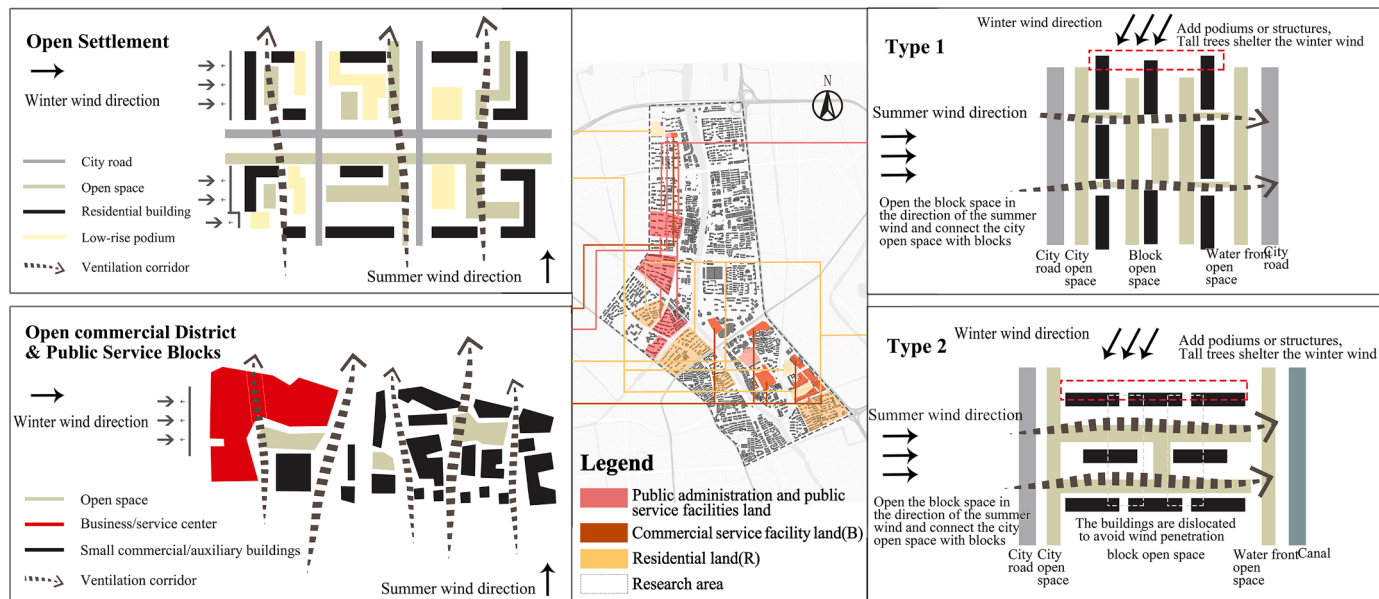


Fig. 10. Schematic diagram of open space planning and reconstruction in the study area.

6. Conclusions

In this study, a simplified PM model and 3D building model (CFD model) were constructed. Wind speed simulations and measurements were conducted for a UVA to verify these models. The results of this study indicate that the constructed models have high simulation accuracy. The model obtained by integrating the constructed PM and WAIE models is applied to the wind field simulation study around the water body, saving the simulation time and improving the simulation efficiency. In this study, the wind environment in the UWA of the Gongshu section of the Beijing–Hangzhou Canal in Hangzhou was finely simulated. In summer, the downwind direction of the 1.5m-height canal in the study area and the pedestrian wind comfort in some historical blocks are poor. Open areas located at heights of 10 and 30 m are potential spaces for ventilation corridors. In winter, the pedestrian wind comfort at a height of 1.5 m is poor, exceeding the comfortable wind speed value, but the area south of Daguan Road has suitable pedestrian wind comfort. Overall, roads were discovered to exhibit the highest ventilation performance, followed by point-like open spaces and porous regions. The river in the study area has the poorest ventilation performance in summer but performs more highly in winter. In addition, the ventilation performance of waterways and roads is related to their orientation and width, which of open spaces is related to their location, and that of porous areas is related to their porosity.

To improve the ventilation environment in the study area in winter and summer, three strategies are proposed for ventilation environment optimization. First, a second level UVC with the study area's canal as the center can be designed by combining the canal, roads, and open spaces. Second, the ventilation in the study area can be enhanced by optimizing its road network, including the integrity and hierarchy of the network. The continuity of the road network should be enhanced, the green spaces on both sides of the main road should be enlarged, and the width of the air duct should be increased. Third, the UWA's open space system can be completed by complementing the ecological functions of the canal. The end of the water system is supplemented by a continuous linear open space, which results in the formation of two layers of wind circulation in the study area. In addition, to promote regional ventilation, high-rise buildings should be reasonably planned, and the development intensity should be distributed rationally. Finally, the development of open spaces and architectural control can reduce the obstruction of wind flow in summer and block cold wind in winter to improve comfort in the outdoor space.

Our research results provided a scientific basis for the larger-scale and more convenient 3D high-precision wind field simulation in UWA and a new direction for developing professional application software. For so many high-density urban living and working spaces in metropolises worldwide, high-precision simulation of ventilation environment makes valuable popularization and application possible to meet the social needs of urban comfortable wind environment. Although this study verified the accuracy and efficiency of the constructed integrated model with the field observation data of a relatively small area of UWA (1.27Km^2), and realized the wind environment of a larger range of UWA (7.91Km^2) complex three-dimensional urban space .The refined simulation finally proved that it has a good application value in wind adaptive planning and design. It can be said that these works provide a technical basis for the subsequent high-precision simulation of urban wind sensitivity. However, the integrated model constructed in this study requires some improvement in some aspects. Although the findings of this study confirm the reliability of the PM model, this model must be expanded to different urban environments. The developed integrated model can be combined with other models, such as vegetation evapotranspiration and pollution diffusion models, in the future for in-depth research. The ventilation performance of different types of space and the factors affecting this performance should be examined by quantifying relevant control variables. In addition, it is a development trend to combine detailed three-dimensional ventilation environment

research with urban planning, design and construction. At the same time, large-scale three-dimensional refined urban wind environment simulation research should also be coupled with other aspects of ecological fields such as thermal environment, water environment, and pollution diffusion.

Declaration of Competing Interest

The authors declare that they have no known competing financial interests or personal relationships that could have appeared to influence the work reported in this paper.

Acknowledgments

The authors acknowledge the National Natural Science Foundation of China (Grant No. 51578482) for financially supporting this study.

Supplementary materials

Supplementary material associated with this article can be found, in the online version, at doi:[10.1016/j.scs.2022.104088](https://doi.org/10.1016/j.scs.2022.104088).

References

- Andersen, L., Corazon, S., & Stigsdotter, U. (2021). Nature exposure and its effects on immune system functioning: A systematic review. *International Journal of Environmental Research and Public Health*, 18(4), 1416. <https://doi.org/10.3390/ijerph18041416>
- Andrejko, O. S., & Sidorenko, Yu. (2019). The study of the influence of the parameters of the porosity of the medium on the effective modulus of elasticity. *Journal of Physics: Conference Series*, 1214(1), Article 012006. <https://doi.org/10.1088/1742-6596/1214/1/012006>
- Cai, Z., Han, G., & Chen, M. (2018). Do water bodies play an important role in the relationship between urban form and land surface temperature? *Sustainable Cities and Society*, 39, 487–498. <https://doi.org/10.1016/j.scs.2018.02.033>
- Chen, H. Q., & Mao, S. M. (1995). Calculation and verification of an universal water surface evaporation coefficient formula. *Advances in Water Science*, 6, 116–120. <https://kns.cnki.net/kns8/defaultresult/indexChinese>.
- De Bruin, H. A. R., & Keijman, J. Q. (1979). The priestley-taylor evaporation model applied to a large, shallow lake in the Netherlands. *Journal of Applied Meteorology*, 18, 898–903. [https://doi.org/10.1175/1520-0450\(1979\)018<0898:TPTEMA>2.0.CO;2](https://doi.org/10.1175/1520-0450(1979)018<0898:TPTEMA>2.0.CO;2)
- Dennison, M., & Berry, J. (1993). *Wetlands: Guide to science, law, and technology* (Chapter 4). Noyes Publications.
- Golany, G. S. (1996). Urban design morphology and thermal performance. *Atmospheric Environment*, 30, 455–465. [https://doi.org/10.1016/1352-2310\(95\)00266-9](https://doi.org/10.1016/1352-2310(95)00266-9)
- Hang, J., & Li, Y. (2012). Macroscopic simulations of turbulent flows through high-rise building arrays using a porous turbulence model. *Building & Environment*, 49, 41–54. <https://doi.org/10.1016/j.buildenv.2011.09.013>
- Hathaway, E. A., & Sharpies, S. (2012). The interaction of rivers and urban form in mitigating the Urban Heat Island effect: A UK case study. *Building & Environment*, 58, 14–22. <https://doi.org/10.1016/j.buildenv.2012.06.013>
- Hong, J. L., & Fu, G. B. (1993). A method of estimation of evaporation from water surface. *Geographical Research*, 12, 55–62. <https://doi.org/10.11821/y1993020007>. Chinese.
- Jauregui, E. (1990). Effects of revegetation and new artificial water bodies on the climate of northeast Mexico City. *Energy & Buildings*, 15(3–4), 447–455. [https://doi.org/10.1016/0378-7788\(90\)90020-J](https://doi.org/10.1016/0378-7788(90)90020-J)
- Jeanjean, A., Hincliffe, G., McMullan, W. A., et al. (2015). A CFD study on the effectiveness of trees to disperse road traffic emissions at a city scale. *Atmospheric Environment*, 120, 1–14. <https://doi.org/10.1016/j.atmosenv.2015.08.003>
- Jiang, Z. X., Liu, J., Song, X. C., et al. (2013). Dynamic simulation analysis on effect of water body on urban region thermal-humid climate. *Building Science*, 29, 85–90. <https://doi.org/10.3969/j.issn.1002-8528.2013.02.018>. Chinese.
- Jin, H., Shao, T., & Zhang, R. L. (2017). Effect of water body forms on microclimate of residential district. *Energy Procedia*, 134, 256–265. <https://doi.org/10.1016/j.egypro.2017.09.615>
- Kang, W. Y., Jiao, J. L., & Wang, J. (2003). Comparative analysis of calculation methods for total solar radiation. *Meteorology and Environmental Science*, 3, 33–37. <https://doi.org/10.3969/j.issn.1673-7148.2008.03.008>. Chinese.
- Li, D. H., Ai, B., & Li, X. (2008a). Research on urban water body mitigation of heat island effect based on remote sensing and GIS: Taking Dongguan City as an example. *Tropical Geography*, 28, 414–418. <https://doi.org/10.3969/j.issn.1001-5221.2008.05.005>. Chinese.
- Li, S. Y., Xuan, C. Y., Li, W., et al. (2008b). Analysis of microclimate effects of water body in a city. *Chinese Journal of Atmospheric Sciences*, 32, 552–560. <https://doi.org/10.3878/j.issn.1006-9895.2008.03.12>. Chinese.
- Li, W. Y. (2000). Research on a nationwide calculation model of water surface evaporation. *Hydrology*, 20, 13–17. doi:CNKI:SUN:SWZZ.0.2000-04-004Chinese.

- Lin, Y., Wang, Z., Chi, Y. J., et al. (2020). Water as an urban heat sink: Blue infrastructure alleviates urban heat island effect in mega-city agglomeration. *Journal of Cleaner Production*, 262, 0959–6526. <https://doi.org/10.1016/j.jclepro.2020.121411>
- Liu, H. Y., Jay, M., & Chen, X. (2021). The role of nature-based solutions for improving environmental quality, health and well-being. *Sustainability*, 13(19), 10950. <https://doi.org/10.3390/su131910950>
- Liu, L. P. (2009). *Research on diesel engine particulate filtration system*. Shandong University. <https://doi.org/10.7666/d.y1565979>
- Ma, J. (2006). *Numerical study of wind environment around building complexes*. Hangzhou, China: Zhejiang University.
- Madsen, O. S. (1974). Wave transmission through porous structures. *Journal of the Waterways, Harbors and Coastal Engineering Division*, 100(3), 169–188. <https://doi.org/10.1016/AWHCAR.0000242>
- Meng, H., & Li, A. G. (2015). Review on the study of layout patterns and greening based on wind environment. *Building Science*, 31, 54–59. <https://doi.org/10.13614/j.cnki.11-1962.tu.2015.02.009>. Chinese.
- Meng, Y., Wang, W., Xu, W. J., Guan, X. J., & Yan, D. H. (2016). Structure construction, evolution analysis and sustainability evaluation of water-ecological-economic system. *Sustainable Cities and Society*, 83, Article 103966. <https://doi.org/10.1016/j.scs.2022.103966>, 2210-6707.
- Min, Q. (2005). Improvement of the wind speed function of Dalton formula. *Hydrology*, 25, 37–41. <https://doi.org/10.3969/j.issn.1000-0852.2005.01.009>. Chinese
- Nie, X., & Qu, X. N. (2017). Research progress of water surface evaporation calculation model. *Rural Economy and Science-Technology*, 31(1), 45–47. <https://doi.org/10.13448/j.cnki.jare.2017.019>
- Park, K., Kim, D., Lee, M., et al. (2017). Analysis of micro-climate on the programs of urban infrastructure regeneration in J city, Republic of Korea. *Urban Forestry & Urban Greening*, 27, 43–49. <https://doi.org/10.1016/j.ufug.2017.06.002>
- Penman, H. L. (1948). Natural evaporation from open water, bare soil and grass. *Proceedings of the Royal Society of London*, 193(1032), 120. <https://doi.org/10.1098/rspa.1948.0037>
- Prévost, J. H. (1980). Mechanics of continuous porous media. *International Journal of Engineering Science*, 18, 787–800. [https://doi.org/10.1016/0020-7225\(80\)90026-9](https://doi.org/10.1016/0020-7225(80)90026-9)
- Priestley, C. H. B., & Taylor, R. J. (1972). On the assessment of surface heat flux and evaporation using large scale parameters. *Monthly Weather Review*, 100, 81–92. [https://doi.org/10.1175/1520-0493\(1972\)100<0081:OTAOOSH>2.3.CO;2](https://doi.org/10.1175/1520-0493(1972)100<0081:OTAOOSH>2.3.CO;2)
- Pu, P. M. (1994). Study on the formula of water surface evaporation and heat dissipation coefficient (1). *Journal of Lake Sciences*, 6, 201–210. <https://doi.org/10.18307/1994.0302> Chinese
- Reyers, B., & Selig, E. R. (2020). Global targets that reveal the social–ecological interdependencies of sustainable development. *Nature Ecology & Evolution*, 4(8), 1011–1019. <https://doi.org/10.1038/s41559-020-1230-6>
- Salim, M. H., Heinke Schlünzen, K., Grawe, D., et al. (2015). Including trees in the numerical simulations of the wind flow in urban areas: Should we care? *Journal of Wind Engineering & Industrial Aerodynamics*, 144, 84–95. <https://doi.org/10.1016/j.jweia.2015.05.004>
- Sebastian, E., & Ellen, B. (2022). High-precision monitoring of urban structures to understand changes in multiple ecosystem services. *Urban Forestry & Urban Greening*, 73, Article 127616. <https://doi.org/10.1016/j.ufug.2022.127616>
- Simiu, E., & Scanlan, R. H. (1992). *The effect of wind on structures: An introduction to wind engineering*. Tongji University Press.
- Song, X. C., Liu, J., & Zhao, Y. (2017). Effect of design factors on the thermal environment in the waterfront area. *Procedia Engineering*, 205, 2677–2682. <https://doi.org/10.1016/j.proeng.2017.10.222>
- Sun, X., Tan, X., Chen, K., et al. (2020). Quantifying landscape-metrics impacts on urban green-spaces and water-bodies cooling effect: The study of Nanjing, China. *Urban Forestry & Urban Greening*, 55, Article 126838. <https://doi.org/10.1016/j.ufug.2020.126838>
- Syafii, N. I., Ichinose, M., Kumakura, E., et al. (2017). Thermal environment assessment around bodies of water in urban canyons: A scale model study. *Sustainable Cities & Society*, 34, 79–89. <https://doi.org/10.1016/j.scs.2017.06.012>
- Syafii, N. I., Ichinose, M., Wong, N. H., et al. (2016). Experimental study on the influence of urban water body on thermal environment at outdoor scale model. *Procedia Engineering*, 169, 191–198. <https://doi.org/10.1016/j.proeng.2016.10.023>
- Szucs, A. (2013). Wind comfort in a public urban space—Case study within Dublin Docklands. *Frontiers of Architectural Research*, 2, 50–66. <https://doi.org/10.1016/j foar.2012.12.002>
- Tanny, J., Cohen, S., Assouline, S., et al. (2008). Evaporation from a small water reservoir: Direct measurements and estimates. *Journal of Hydrology*, 351, 218–229. <https://doi.org/10.1016/j.jhydrol.2007.12.012>
- Teng, K. (2011). Optimization of water surface evaporation model. *Chinese Journal of Water Resources and Water Engineering*, 22, 163–166. doi:CNKI:SUN:XBSZ.0.2011-01-041Chinese.
- Wang, H. (1992). The Change in velocity of air flows over inland water. *Journal of Tropical Meteorology*, 1, 27–34. Chinese.
- Wang, W. W., Wang, D., Chen, H., et al. (2022). Identifying urban ventilation corridors through quantitative analysis of ventilation potential and wind characteristics. *Building and Environment*, 108943, 0360–1323. <https://doi.org/10.1016/j.buildenv.2022.108943>
- Xue, Z. S., Hou, G. L., Zhang, Z. S., et al. (2019). Quantifying the cooling-effects of urban and peri-urban wetlands using remote sensing data: Case study of cities of Northeast China. *Landscape and Urban Planning*, 182, 92–100. <https://doi.org/10.1016/j.landurbplan.2018.10.015>
- Yang, Z., Yu, L., & Liu, J. (2015). Layout study on riverside residential building: Analysis of thermal environment simulation. *Southern Architecture*, 6, 74–75. <https://doi.org/10.3969/j.issn.1000-0232.2015.06.074>. Chinese
- Zhang, J., Zou, H. F., Li, S., et al. (2016a). Simulation study of particulate matter adsorbed by greening trees as porous media. *Building Technology Development*, 43, 20–22. doi:CNKI:SUN:JZKF.0.2016-08-015Chinese.
- Zhang, Y. L., Qin, B. Q., Chen, W. M., et al. (2003). Climatological calculation and characteristic analysis of total solar radiation in Taihu Lake and Wuxi area. *Chinese Journal of Applied Meteorology*, 3, 339–347. <https://doi.org/10.3969/j.issn.1001-7313.2003.03.009>. Chinese.
- Zhang, Y. W., Gu, Z. L., & Zhou, D. (2016b). Simulation on urban wind environment based on local climate zones and its parameterization. *Journal of Earth Environment*, 7, 480–486. <https://doi.org/10.7515/JEE201605004>. +493Chinese.